Article

High-density switchable skyrmion-like polar nanodomains integrated on silicon

https://doi.org/10.1038/s41586-021-04338-w

Received: 24 January 2021

Accepted: 10 December 2021

Published online: 2 March 2022

Check for updates

Lu Han[1,2], Christopher Addiego[3], Sergei Prokhorenko[4], Meiyu Wang[1,2], Hanyu Fu[1,2], Yousra Nahas[4], Xingxu Yan[5,6], Songhua Cai[7], Tianqi Wei[1,2], Yanhan Fang[1,2], Huazhan Liu[1,2], Dianxiang Ji[7], Wei Guo[1,2], Zhengbin Gu[1,2], Yurong Yang[1,2], Peng Wang[1,2,8], Laurent Bellaiche[4], Yanfeng Chen[1,2], Di Wu[1,2]✉, Yuefeng Nie[1,2]✉ & Xiaoqing Pan[3,5,6]✉

Topological domains in ferroelectrics[1–5] have received much attention recently owing to their novel functionalities and potential applications[6,7] in electronic devices. So far, however, such topological polar structures have been observed only in superlattices grown on oxide substrates, which limits their applications in silicon-based electronics. Here we report the realization of room-temperature skyrmion-like polar nanodomains in lead titanate/strontium titanate bilayers transferred onto silicon. Moreover, an external electric field can reversibly switch these nanodomains into the other type of polar texture, which substantially modifies their resistive behaviours. The polar-configuration-modulated resistance is ascribed to the distinct band bending and charge carrier distribution in the core of the two types of polar texture. The integration of high-density (more than 200 gigabits per square inch) switchable skyrmion-like polar nanodomains on silicon may enable non-volatile memory applications using topological polar structures in oxides.

Recent discoveries have shown that ferroelectric polarization can form complex topological structures, including flux-closure domains[1], vortices[2], labyrinthine domains[3,8], polar skyrmions[4], merons[5] and others[9–12]. Owing to the polarization and charge distribution discontinuity, non-uniform polar textures could give rise to emergent functionalities that are distinct from the bulk domains[6,7,13,14], with the potential for novel applications in next-generation electronic devices. For instance, an array of nanometre-size polar skyrmions, if they can be read and written easily, will be promising for ultrahigh-density recording well above terabits per square inch[15,16]. Despite these rich physical properties and promising potential applications, it is still challenging to integrate these topological textures into silicon-based technology as they are mostly observed in superlattices grown on single-crystal oxide substrates.

Here we demonstrate the observation of high-density (approximately 200 Gbit per square inch) skyrmion-like polar nanodomains in freestanding $(PbTiO_3)_{20}/(SrTiO_3)_{10}$ bilayers transferred onto silicon ($PbTiO_3$, lead titanate (PTO); $SrTiO_3$, strontium titanate (STO)). These nanodomains are switchable under an external electric field, with the resistance greatly modulated by reversibly switching between the two types of polarization structure, providing a route to design non-volatile ferroelectric memories using topological polar structures.

A series of $(PbTiO_3)_m/(SrTiO_3)_n$ (where m and n are the number of unit cells) bilayers were grown on $SrTiO_3$(001) substrates using water-soluble strontium aluminate ($Sr_3Al_2O_6$; SAO) as the sacrificial layer[17] by reactive molecular beam epitaxy. The bilayers were then released by dissolving the SAO buffer layer in deionized water and laminated on a platinized silicon (Si) (001) substrate (Fig. 1a). More details about the film growth, transfer and characterizations can be found in the Methods and Extended Data Fig. 1.

Topological polar structures

The domain structures of the bilayers were characterized by vector piezoelectric force microscopy[18,19]. The pristine state shows two types of round-shape nanodomain, which are highlighted by red and blue circles in Fig. 1b, with their zoom-in PFM images shown in Fig. 1c, d, respectively. Interestingly, these polar textures are not directly related to the topography of the samples. For the red-circled nanodomains, the vertical PFM (VPFM) amplitude image shows a ring-shape dark contrast and the phase image shows a 180° phase inversion between the out-of-plane polarization at the centre and that in the surrounding background region. The lateral PFM (LPFM) phase image shows a half-violet and half-yellow contrast and the amplitude image shows round-shape bright contrast split by a dark line, indicating a phase inversion of the lateral polarization component along the direction perpendicular to the cantilever. By rotating the sample clockwise for a set of given angles (Fig. 2a), the dark line in the LPFM amplitude image rotates continuously with the cantilever and the phase image always shows a 180° phase inversion of the polarizations between the left side and right side of the cantilever, which implies that the in-plane polarization has a rotation symmetry about the centre of the nanodomains. Following the method proposed in previous studies[18,19], our

[1]National Laboratory of Solid State Microstructures, Jiangsu Key Laboratory of Artificial Functional Materials, College of Engineering and Applied Sciences, Nanjing University, Nanjing, People's Republic of China. [2]Collaborative Innovation Center of Advanced Microstructures, Nanjing University, Nanjing, People's Republic of China. [3]Department of Physics and Astronomy, University of California, Irvine, CA, USA. [4]Physics Department and Institute for Nanoscience and Engineering, University of Arkansas, Fayetteville, AR, USA. [5]Department of Materials Science and Engineering, University of California, Irvine, CA, USA. [6]Irvine Materials Research Institute, University of California, Irvine, CA, USA. [7]Department of Applied Physics, The Hong Kong Polytechnic University, Hong Kong SAR, People's Republic of China. [8]Department of Physics, University of Warwick, Coventry CV4 7AL, UK. ✉e-mail: diwu@nju.edu.cn; ynie@nju.edu.cn; xiaoqing.pan@uci.edu

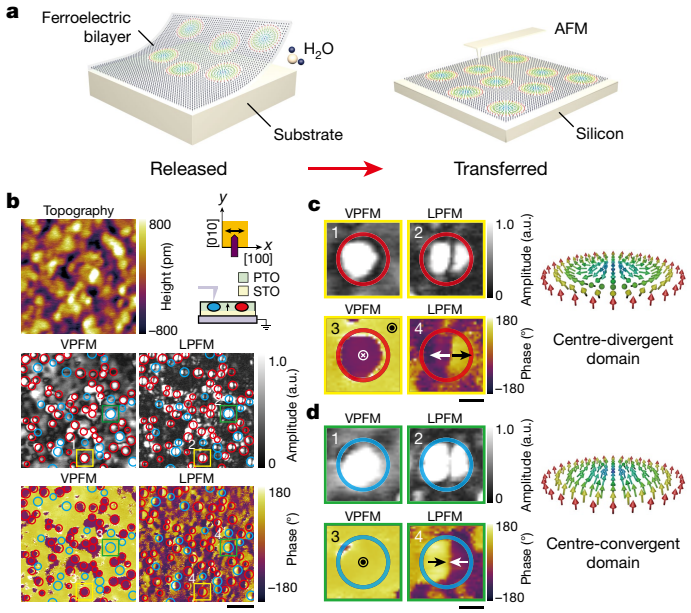

Fig. 1 | High-density polar nanodomains in a PTO_{20}/STO_{10} bilayer from PFM measurements. a, Schematic description of the release and transfer process of oxide membranes. **b**, Topography, VPFM amplitude, VPFM phase, LPFM amplitude and LPFM phase images for the freestanding PTO/STO bilayers transferred onto a platinized silicon substrate. The two types of topological nanodomain observed in the bilayer are marked by red and blue circles. The top right schematic drawing illustrates the sample and scan geometry, showing that the cantilever is parallel to the *y* axis ([010] direction), and the contrast in the LPFM images reflects the *x* component of polarization vectors (along the [100] direction). All the images are from the same region. Scale bar, 100 nm. **c**, **d**, Zoomed-in PFM images for the two types of nanodomain: centre-divergent domain (**c**) and centre-convergent domain (**d**). Scale bars, 30 nm.

in-plane vector PFM mapping shows that the red-circled nanodomains have a centre-divergent pattern (Fig. 2b). Calculating the divergence of these nanodomains enables us to distinguish the centre-divergent domains between the four-domain vortices and skyrmion-like bubbles (Extended Data Fig. 2). Combining the out-of-plane and the in-plane polarization information, the polar textures of the red-circled nanodomains are depicted schematically in Fig. 1c, which indicates that these red-circled nanodomains are Néel-type skyrmion-like nanodomains. More details about the vector PFM mapping can be found in the Methods and Extended Data Fig. 3.

In contrast, the blue-circled nanodomains show no inversion of the out-of-plane polarizations and their in-plane polarizations show a centre-convergent pattern (Figs. 1d, 2a, b), which indicates that they are not Néel-type skyrmions. As will be shown later, these centre-convergent nanodomains are closely related to the centre-divergent nanodomains but show different resistive behaviours. Interestingly, throughout the PFM measurements, both types of nanodomain show a central symmetry and are quite stable, which are essential for further manipulation and application as a functional unit in devices.

To confirm that the polar textures observed in PFM measurements are indeed topological structures, we also performed polarization mapping via four-dimensional scanning transmission electron microscopy (4D STEM) using a nanoscale electron probe. The polarization in ferroelectric materials can be determined from convergent beam electron diffraction (CBED) patterns based on the difference in intensity distribution between conjugate pair diffraction disks[4,20,21]. Our 4D STEM results confirm both the centre-divergent-type (Fig. 2c, d) and the centre-convergent-type (Extended Data Fig. 4a) polar nanodomains. The typical size (about 5–9 nm) of the skyrmion-like nanodomains is smaller than that observed in the PFM measurements, which may be related to the resolution of the PFM technique limited by the tip size (Extended Data Fig. 5)[22,23]. It is also noted that it is unlikely that these polar nanodomains are driven by extrinsic effects[24,25] as no clear lattice or charge defects have been detected in high-angle annular dark-field scanning transmission electron microscopy (HAADF STEM), position-averaged CBED and charge density maps (Extended Data Fig. 4).

Effective Hamiltonian simulations

The stabilization of such skyrmion-like nanodomains is supported by our effective Hamiltonian model simulations[3,15,26,27]. As shown in Fig. 3, the simulated freestanding bilayer structure corresponds to round-shaped downwards-oriented nanodomains with a diameter of 10 to 15 unit cells (5 nm to 7 nm) embedded in an upwards-polarized matrix, consistent with the size observed in the 4D STEM data. In accordance with experimental observations, we also find that the in-plane polarization within such nanodomains has a centre-divergent character (Fig. 3a) with the two-dimensional winding number[28] equal to one for each domain. The origin of this non-trivial in-plane topology can be traced back to asymmetric screening conditions for the PTO layer[29]. Namely, the poor screening of bound charges at the PTO/STO interface induces Néel polarization rotation in planes passing through the axis perpendicular to the interface. As a result, the nanodomain boundary has a rounded closure in the vicinity of the STO layer that does not reach the STO surface (Fig. 3b–d). Within the first unit-cell layer of PTO above the STO surface, the dipoles are aligned along the polarization of the embedding matrix, but also feature a centre-divergent pattern formed by in-plane dipolar components. The second layer above the STO surface reveals a classical Néel skyrmion pattern with a downwards-oriented core (Fig. 3c, d) at the tip of the nanodomain boundary. Moving farther away from the interface, the core of the nanodomain first enlarges and the Néel rotations disappear six layers above the interface, leading to a sharp 180° circular domain-wall boundary of fixed radius. At the free PTO interface, the dipoles are aligned perpendicular to the surface because of the ideal electrostatic screening conditions. More details about the topological characterization of the nanodomains can be found in the Methods and Extended Data Fig. 6.

Interestingly, our simulations indicate that another state can be also stabilized by switching only the top part of the dipoles from pointing downwards to upwards as the surrounding background (Fig. 2e), which explains the observation of centre-convergent nanodomains. As shown in Extended Data Fig. 7, above and below the resulting Néel bubble skyrmion[11,30,31], the local dipoles lean towards and away from the central revolution axis, respectively. However, the centre-divergent distortion below the domain is not fully developed because of the STO layer. As a result, in accordance with our PFM and 4D STEM experiments, the local polarization averaged over the bilayer thickness has a centre-convergent character.

The stability of Néel skyrmion-like polar nanodomains crucially depends on the thickness of the PTO and the STO layers. The STO layer is essential to create a strong depolarizing field at the origin of the non-trivial dipolar rotations. Moreover, it elastically constrains the PTO layer and gives rise to a built-in field, both of which prevent the development of in-plane-oriented tetragonal domains while also breaking the remaining Z_2 tetragonal symmetry[30]. The stabilization of these nanodomains is subject to a delicate balance of these factors that can be changed by tuning the volume fraction of PTO. For instance, considering the STO thickness fixed and decreasing the number of PTO layers gives rise to two competing mechanisms. The first mechanism is related to a drop in the coercive field magnitude, and, consequently, a more pronounced role of the built-in field. Such a mechanism favours a homogeneously polarized state. The competing mechanism is related to enhanced in-plane clamping of PTO on increasing the STO volume

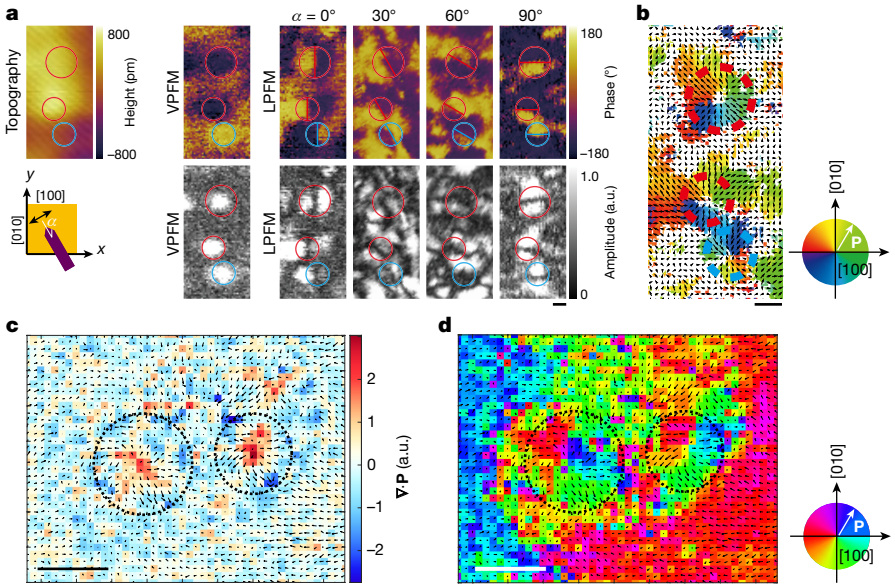

Fig. 2 | Polarization mapping of polar nanodomains in a PTO_{20}/STO_{10} bilayer by vector PFM and 4D STEM. a, Topography, LPFM phase, LPFM amplitude, VPFM amplitude and VPFM phase images for the same region measured with four various cantilever orientations ($\alpha = 0°$, $\alpha = 30°$, $\alpha = 60°$ and $\alpha = 90°$, where α is the angle between the cantilever and [010] axis). Scale bar, 30 nm. **b**, Polarization texture of the nanodomains in the same region as **a** measured by vector PFM, showing the coexistence of centre-convergent and centre-divergent domains, which are marked by dotted red and blue circles, respectively. Scale bar, 30 nm. **c**, **d**, Polarization mapping by 4D STEM. Polarization mapping is calculated from conjugate pair asymmetry. Two centre-divergent skyrmion-like structures are highlighted by the circles. The background in **c** shows the divergence of the polarization field. The background in **d** shows the vector direction. Scale bar, 5 nm. Note that the larger size of the nanodomains measured by PFM is most likely related to the tip size (about 20 nm).

fraction which, inversely, increases the transition temperature and the coercive field magnitude.

The importance of the PTO layer thickness as the parameter governing the stability of the skyrmion-like nanodomains is consistent with our experimental observations that skyrmion-like textures exist only in $(PbTiO_3)_{20}/(SrTiO_3)_{10}$ films among $(PbTiO_3)_n/(SrTiO_3)_{10}$ ($n = 12$, $n = 16$ and $n = 20$) bilayers (Extended Data Fig. 8a–c). Indeed, the X-ray diffraction images indicate a sharp change in the lattice parameters of the 20-unit-cell freestanding PTO film with or without a 10-unit-cell STO layer (Extended Data Fig. 8d–g). After transfer, the polarization in the PTO layer has a tendency to rotate from the out-of-plane direction to the in-plane direction owing to the strong depolarization field, thus increasing the in-plane lattice parameter of PTO. Therefore, the STO layer will introduce an elastic constraint to the PTO. This exact elastic constraint value can be varied by manipulating the thickness ratio of these two layers ($z = t_{PTO}/t_{STO}$) to tune the competition between the elastic energy of these two layers. The significant reduction of the tetragonality (from 1.04 to 1.01) by adding the dielectric STO layer provides a suitable situation where skyrmion-like nanodomains can exist.

Switchable and resistive behaviours

It is of great interest to explore whether the skyrmion-like nanodomains are tunable and how these two types of nanodomain will respond to external electric field stimuli. To this end, we apply a scanning tip bias of ±5 V to a 500 × 250 nm^2 region of a $(PbTiO_3)_{20}/(SrTiO_3)_{10}$ bilayer (Extended Data Fig. 9). The PFM data were taken under an a.c. amplitude of 500 mV after applying the ±5-V d.c. voltage, which indicates the non-volatile switching behaviour of these nanodomains. Remarkably, only the centre-divergent (centre-convergent) type of nanodomain is observed after scanning with a positive (negative) bias, which indicates that these two types of nanodomain can be reversibly switched to their counterparts by an external electric field. The reversible switching between these two types of nanodomain indicates that they are closely related to each other as revealed by PFM, 4D STEM and effective Hamiltonian model simulations. Ideally, two equivalent Néel-type skyrmion-like states should be stabilized by simply reversing the polarization of each electric dipole if the material system is symmetric. However, consistent with our computational simulations, there is inherent inversion-symmetry breaking in the PTO/STO bilayer along the out-of-plane direction, giving rise to an upwards background polarization most likely owing to the existence of a built-in electric field at the interface[32]. Owing to this built-in electric field, the external electric field applied by the tip can only reverse part of the dipoles and convert these two types of nanodomain reversibly. We also transferred the freestanding bilayer onto a phosphorous-doped silicon substrate and etched the film into quadrate patterns via a standard electron beam lithography process. As shown in Extended Data Fig. 10, the topological nanodomains still exist, which indicates that the freestanding film and the skyrmion-like nanodomains can be integrated with silicon and survive typical processing steps used in silicon device fabrication.

To explore the potential application in resistive memories, we also investigated the resistive behaviours of these topological nanodomains using conductive atomic force microscopy (CAFM) as shown in Fig. 4. The measured current in the core of the centre-convergent polar nanodomains is similar to the insulating surrounding background area, making this type of topological domain indistinguishable from the matrix. Strikingly, for the centre-divergent polar nanodomains, the core shows a two-orders-of-magnitude enhancement of the conductivity, with a current up to 10^2 pA at +5-V bias. Also, these distinct resistive states can be reversibly switched by applying an electric field to switch between the two types of polar nanodomain. As shown in Fig. 4b, after writing polar nanodomains on the bilayer by applying a +5-V bias on the tip, high-density round-shape nanodots with a high current value are observed in the current map. After switching the centre-divergent polar nanodomains to centre-convergent nanodomains by a scan with −5-V bias, the round-shape high-current nanodots disappear. Owing to the existence of an insulating STO layer (approximately 4 nm), we need relatively high voltages (±5 V)

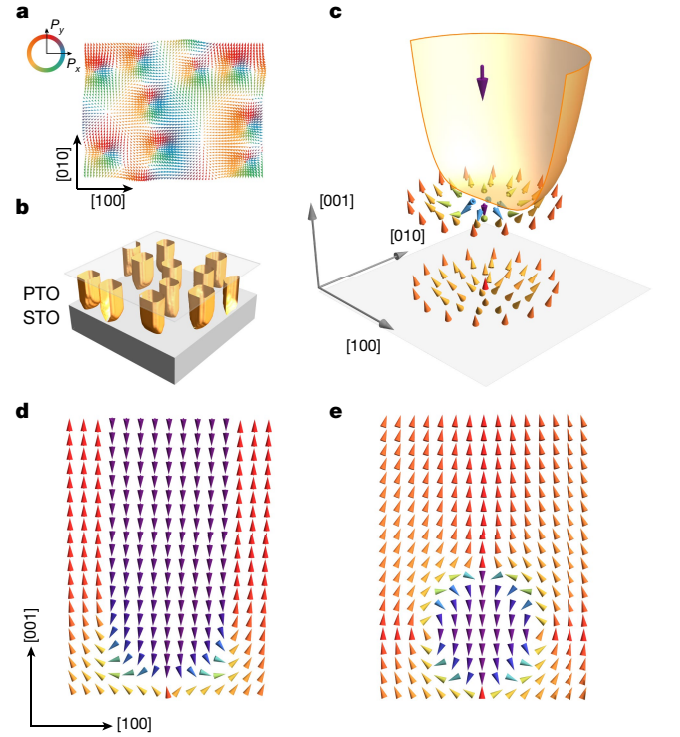

Fig. 3 | Effective Hamiltonian model simulations of skyrmion-like nanodomains in PTO/STO bilayers. a, The simulated in-plane polarization pattern within a 50 × 64-unit-cell part of the supercell. The arrows correspond to the in-plane projection of local dipoles averaged over the bilayer thickness. **b**, The shape of the simulated centre-divergent nanodomains. The yellow surfaces show the domain boundaries. **c**, Schematic dipolar structure of the centre-divergent nanodomains at the STO/PTO interface. The arrows represent the dipoles in the first two layers above the interface indicated by a grey plane. **d**, **e**, The (010) cross-section of a typical centre-divergent nanodomain (**d**) and a centre-convergent nanodomain (**e**) obtained from simulations. The arrows represent unit-cell dipoles coloured according to their out-of-plane component.

to tunnel the energy barrier to obtain low-noise data when measuring the current maps, which could switch the nanodomains and alter the original information (Extended Data Fig. 9). Nonetheless, the current maps of these two different domains show different resistive states (Fig. 4b). At present, PFM and STEM are the techniques to read the non-volatile information. To obtain reliable non-destructive reading of the resistive states, a possible solution is to lower the tunnelling voltage by reducing the thickness of the STO layer while maintaining the skyrmion-like nanodomains. Using other techniques that can measure the resistive states without applying high external d.c. voltage may also be helpful. This reversible switching of the nanodomain types and resistive states provides a possible route to the design of resistive memory devices based on topological polar nanodomains[33].

The possible mechanism to explain the observed phenomena is schematically shown in Fig. 4c. The bilayer system sandwiched by the bottom electrode and the conducting tip forms a junction and its resistance can be tuned if the nanodomains can be switched between insulating states and conducting states. Similar to the highly conducting channels observed in the ferroelectric domain walls[18,34–36], it is not surprising to expect enhanced conductivity in the vicinity of the core of centre-divergent nanodomains as there is such a large polarization divergence. In contrast, owing to the absence of inversion of the out-of-plane polarization in the centre-convergent nanodomains, the polarization divergence near its core is lower as the electric dipoles do not need to experience the fully in-plane orientation to bridge the antiparallel orientations at the core and surrounding background. As such, the two types of nanodomain lead to different barrier widths and band diagrams of the junction, giving rise to distinct resistive states (Fig. 4c). As shown in our PFM, 4D STEM and computational simulations, the lateral size of the polar nanodomains is about 30 nm or smaller, corresponding to a pixel density of about 200 Gbit per square inch or higher, which is higher than that in commercialized memory devices and an artificially synthesized array of ferroelectric nanodots[37,38].

Conclusion

In summary, we report the observation of two types (centre divergent and centre convergent) of skyrmion-like polar nanodomain in $PbTiO_3$/$SrTiO_3$ bilayers transferred onto silicon, which can be converted to each other by applying an external electric field. High-density resistive memories based on these topological nanodomains have been demonstrated and the 'on' and 'off' states can be controlled by switching the type of nanodomain. There are several unique advantages of this type of polar texture integrated on silicon. (1) As there is only a single layer

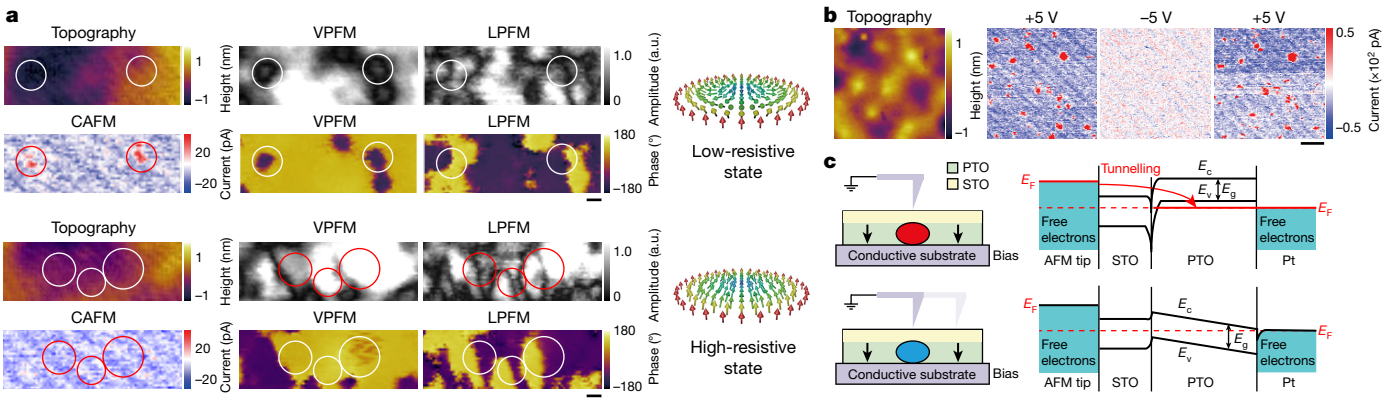

Fig. 4 | Resistive behaviours of the polar nanodomains integrated on silicon. a, Topography, VPFM and LPFM images, and CAFM current maps collected at the same area after a +5-V scan (top two rows) and a −5-V scan (bottom two rows) to switch the polar domains between centre-divergent and centre-convergent nanodomains. The CAFM images show that the centre-divergent nanodomains are in a low-resistive state and that the centre-convergent nanodomains are in a high-resistive state. Scale bar, 20 nm. **b**, Reversible switching between the low-resistive, centre-divergent and high-resistive, centre-convergent states by +5-V and −5-V bias voltage. Scale bar, 50 nm. **c**, Schematic band diagram of the two different types of polar structure. Top: with significant polarization divergence near the core of the centre-divergent nanodomain, hole-like charge carriers are injected, which shifts the Fermi level into the valence band. Thus, the barrier width of the junction is much narrower, resulting in a low-resistive state. Bottom: in contrast, owing to the small polarization divergence, the centre-convergent nanodomain remains in a high-resistive state. E_F, Fermi level; E_c, conduction band; E_v, valence band; E_g, bandgap).

of skyrmion-like nanodomains instead of multiple layers of interacting skyrmions, it is easier to switch each individual nanodomain by an external electric field, allowing the effectively 'write' operation. Also, without the interference between multilayers of nanodomains, it enables the direct mapping of the polarization patterns by PFM measurements, which is actually a non-destructive 'read' operation. (2) As it is a direct measurement of the resistive state, this 'read' operation can be much faster than the conventional ferroelectric random-access memory where the read process is destructive, necessitating a write-after-read architecture. (3) More importantly, this unique structure can be integrated on silicon wafers. The integration of high-density switchable skyrmion-like polar nanodomains on silicon may enable non-volatile memory applications using topological polar structures in oxides.

Online content

Any methods, additional references, Nature Research reporting summaries, source data, extended data, supplementary information, acknowledgements, peer review information; details of author contributions and competing interests; and statements of data and code availability are available at https://doi.org/10.1038/s41586-021-04338-w.

1. Tang, Y. L. et al. Observation of a periodic array of flux-closure quadrants in strained ferroelectric $PbTiO_3$ films. *Science* **348**, 547–551 (2015).
2. Yadav, A. K. et al. Observation of polar vortices in oxide superlattices. *Nature* **530**, 198–201 (2016).
3. Nahas, Y., Prokhorenko, S., Fischer, J., Xu, B. & Bellaiche, L. Inverse transition of labyrinthine domain patterns in ferroelectric thin films. *Nature* **577**, 47–51 (2020).
4. Das, S. et al. Observation of room-temperature polar skyrmions. *Nature* **568**, 368–372 (2019).
5. Wang, Y. J. et al. Polar meron lattice in strained oxide ferroelectrics. *Nat. Mater.* **19**, 881–886 (2020).
6. Seidel, J. et al. Conduction at domain walls in oxide multiferroics. *Nat. Mater.* **8**, 229–234 (2009).
7. Zubko, P. et al. Negative capacitance in multidomain ferroelectric superlattices. *Nature* **534**, 524–528 (2016).
8. Eliseev, E. A. et al. Labyrinthine domains in ferroelectric nanoparticles: manifestation of a gradient-induced morphological transition. *Phys. Rev. B* **98**, 054101 (2018).
9. Wei, X. K. et al. Neel-like domain walls in ferroelectric $Pb(Zr,Ti)O_3$ single crystals. *Nat. Commun.* **7**, 12385 (2016).
10. Prokhorenko, S., Nahas, Y. & Bellaiche, L. Fluctuations and topological defects in proper ferroelectric crystals. *Phys. Rev. Lett.* **118**, 147601 (2017).
11. Zhang, Q. et al. Nanoscale bubble domains and topological transitions in ultrathin ferroelectric films. *Adv. Mater.* **29**, 1702375 (2017).
12. Peters, J. J. P., Apachitei, G., Beanland, R., Alexe, M. & Sanchez, A. M. Polarization curling and flux closures in multiferroic tunnel junctions. *Nat. Commun.* **7**, 13484 (2016).
13. Xu, R., Karthik, J., Damodaran, A. R. & Martin, L. W. Stationary domain wall contribution to enhanced ferroelectric susceptibility. *Nat. Commun.* **5**, 3120 (2014).
14. Wada, S., Yako, K., Yokoo, K., Kakemoto, H. & Tsurumi, T. Domain wall engineering in barium titanate single crystals for enhanced piezoelectric properties. *Ferroelectrics* **334**, 17–27 (2006).
15. Naumov, I. I., Bellaiche, L. & Fu, H. Unusual phase transitions in ferroelectric nanodisks and nanorods. *Nature* **432**, 737–740 (2004).
16. Stachiotti, M. G. & Sepliarsky, M. Toroidal ferroelectricity in $PbTiO_3$ nanoparticles. *Phys. Rev. Lett.* **106**, 137601 (2011).
17. Lu, D. et al. Synthesis of freestanding single-crystal perovskite films and heterostructures by etching of sacrificial water-soluble layers. *Nat. Mater.* **15**, 1255–1260 (2016).
18. Kim, K. E. et al. Configurable topological textures in strain graded ferroelectric nanoplates. *Nat. Commun.* **9**, 403 (2018).
19. Kim, J., You, M., Kim, K.-E., Chu, K. & Yang, C.-H. Artificial creation and separation of a single vortex–antivortex pair in a ferroelectric flatland. *npj Quantum Mater.* **4**, 29 (2019).
20. Tsuda, K., Yasuhara, A. & Tanaka, M. Two-dimensional mapping of polarizations of rhombohedral nanostructures in the tetragonal phase of $BaTiO_3$ by the combined use of the scanning transmission electron microscopy and convergent-beam electron diffraction methods. *Appl. Phys. Lett.* **103**, 082908 (2013).
21. Yadav, A. K. et al. Spatially resolved steady-state negative capacitance. *Nature* **565**, 468–471 (2019).
22. Kalinin, S. V. et al. Spatial resolution, information limit, and contrast transfer in piezoresponse force microscopy. *Nanotechnology* **17**, 3400–3411 (2006).
23. Tian, L. et al. Nanoscale polarization profile across a 180° ferroelectric domain wall extracted by quantitative piezoelectric force microscopy. *J. Appl. Phys.* **104**, 074110 (2008).
24. Lee, D. et al. Emergence of room-temperature ferroelectricity at reduced dimensions. *Science* **349**, 1314–1317 (2015).
25. Kim, S. D., Hwang, G. T., Song, K., Chang, K. J. & Choi, S. Y. Inverse size-dependence of piezoelectricity in single $BaTiO_3$ nanoparticles. *Nano Energy* **58**, 78–84 (2019).
26. Zhong, W., Vanderbilt, D. & Rabe, K. M. Phase transitions in $BaTiO_3$ from first principles. *Phys. Rev. Lett.* **73**, 1861–1864 (1994).
27. Bellaiche, L., Garcia, A. & Vanderbilt, D. Finite-temperature properties of $Pb(Zr_{1-x}Ti_x)O_3$ alloys from first principles. *Phys. Rev. Lett.* **84**, 5427–5430 (2000).
28. Mermin, N. D. The topological theory of defects in ordered media. *Rev. Mod. Phys.* **51**, 591–648 (1979).
29. Prosandeev, S. & Bellaiche, L. Asymmetric screening of the depolarizing field in a ferroelectric thin film. *Phys. Rev. B* **75**, 172109 (2007).
30. Nahas, Y. et al. Topology and control of self-assembled domain patterns in low-dimensional ferroelectrics. *Nat. Commun.* **11**, 5779 (2020).
31. Kornev, I., Fu, H. & Bellaiche, L. Ultrathin films of ferroelectric solid solutions under a residual depolarizing field. *Phys. Rev. Lett.* **93**, 196104 (2004).
32. Hsing, G. H.-C. *Strain and Defect Engineering for Tailored Electrical Properties in Perovskite Oxide Thin Films and Superlattices.* PhD Thesis, State Univ. New York at Stony Brook (2017).
33. Edwards, D. et al. Giant resistive switching in mixed phase $BiFeO_3$ via phase population control. *Nanoscale* **10**, 17629 (2018).
34. Crassous, A., Sluka, T., Tagantsev, A. K. & Setter, N. Polarization charge as a reconfigurable quasi-dopant in ferroelectric thin films. *Nat. Nanotechnol.* **10**, 614–618 (2015).
35. Ma, J. et al. Controllable conductive readout in self-assembled, topologically confined ferroelectric domain walls. *Nat. Nanotechnol.* **13**, 947–952 (2018).
36. Zhang, Q. et al. Deterministic switching of ferroelectric bubble nanodomains. *Adv. Funct. Mater.* **29**, 1808573 (2019).
37. Li, Z. et al. High-density array of ferroelectric nanodots with robust and reversibly switchable topological domain states. *Sci. Adv.* **3**, e1700919 (2017).
38. Ding, L. L. et al. Characterization and control of vortex and antivortex domain defects in quadrilateral ferroelectric nanodots. *Phys. Rev. Mater.* **3**, 104417 (2019).

Methods

Sample growth

A water-soluble SAO layer was grown first on a (001) STO single-crystalline substrate (MTI Corp.) followed by the growth of STO and PTO by a DCA Dual R450 Oxide MBE system. The SAO and STO films were grown with an oxidant (10% O_3 and 90% O_2) background pressure p_{O_2} of 1×10^{-6} torr and at $T_{substrate}$ = 950 °C in a layer-by-layer growth mode, of which the thickness was monitored by reflection high-energy electron diffraction oscillations. The PTO films were grown with an oxidant (distilled O_3) p_{O_2} of 2×10^{-5} torr and at $T_{substrate}$ = 625 °C. Owing to the volatility of lead, PTO films were grown in adsorption-controlled mode with a fixed lead:titanium flux ratio of 13:1, and the thickness was controlled by the shutter time of titanium evaporation source.

Structure characterizations

The crystal structure was examined by a high-resolution four-circle X-ray diffractometer using a Bruker D8 Discover instrument. The incident X-ray is from Cu K_α emission and has a wavelength of 1.5418 Å.

Selected area electron diffraction and S/TEM experiments

Selected area electron diffraction patterns were acquired on an FEI Tecnai F20 TEM at 200 kV from a flat area of the samples suspended on holey carbon films or microcarbon grids. A low electron beam current (0.045 nA) and a short exposure time (2.0 s) were used to reduce the electron beam damage. The probe convergence angle on Titan was 25 mrad, and the angular range of the HAADF detector was from 79.5 mrad to 200 mrad.

4D STEM measurements

The TEM samples were prepared by transferring freestanding PTO/STO bilayers to a copper grid with a holey carbon support. The 4D STEM data were collected on a JEOL JEM-ARM300F at 300 kV. The CBED patterns were recorded on a Gatan Oneview at 1,024 × 1,024 resolution running at 200 fps with 0.5-nm pixel size. A convergence angle of 2.4 mrad was used so that the diffraction disks from the (001) plane were well separated.

To determine the polarization, we used the intensity distribution of conjugate pair diffraction disks (also called Friedel pair disks). When there is no polarization present, the intensity distribution in the Friedel pair disks will be symmetric, reflecting the inversion symmetry of the structure. The polarization in PTO breaks this symmetry, so the Friedel pair disks will have an asymmetric intensity distribution. We quantified the asymmetric intensity distribution in each CBED pattern by calculating the centre of mass (COM) of each {200} family diffraction disk. The COM from (200) and ($\bar{2}$00) were averaged together and a reference position was calculated as the average of the combined (200)/($\bar{2}$00) COM from all CBED patterns in the 4D dataset. The shift in the combined (200)/($\bar{2}$00) COM away from the reference point was then taken as the polarization along [100]. The polarization along [010] was calculated analogously from the (020) and (0$\bar{2}$0) diffraction disks.

As the samples were imaged from [001], the PTO and STO layers did overlap in projection. However, as STO is unpolarized, its contribution to the COM does not change with position and will be removed by subtracting the reference position.

PFM measurements

The local piezoelectric and ferroelectric properties of freestanding films on a platinum-coated silicon wafer were examined using an Asylum Research MFP-3D Origin+ scanning probe microscope. NanoWorld EFM platinum/iridium-coated tips (2.8 N m^{-1} in force constant) were used in the PFM measurements. Hysteresis loops were collected in the dual a.c. resonance tracking mode[39]. The vector PFM measurements were carried out by following the method reported previously[18,19] and are schematically shown in Extended Data Fig. 3. As the LPFM technique relies on the torsional vibration mode of the cantilever, only the polarization component projected to the in-plane axis perpendicular to the cantilever is distinguished (Extended Data Fig. 3a). In other words, if the cantilever is parallel to the *y* axis, LPFM measures only the polarization component along the *x* axis. At the region with zero *x* components, there is no torsional vibration.

CAFM measurements

The CAFM experiments were performed with an Asylum ORCA cantilever holder with a gain of 1×10^{-9} V A^{-1}. The bias voltage was applied to the sample and the tip was virtually grounded for all measurements. Current–voltage data were collected with a triangular voltage shape (ramp of 3 V s^{-1}, 2,000 points per second).

Effective Hamiltonian model simulations

In our simulations, the PTO layer is described by the effective Hamiltonian model of bulk PTO[40]. The crystalline structure is characterized using the local mode representation of electric dipoles, the displacements of A-site cations parametrizing the inhomogeneous strain in each unit cell and the six-component homogeneous strain tensor[41]. The PTO effective Hamiltonian comprises the eighth-order polynomial on-site energy terms, short-range and long-range local mode interactions, as well as local mode–strain coupling and the elastic energy. The STO layer is assumed to be a dielectric slab with a constant electric permittivity of $\epsilon = 10$. Furthermore, we take into account homogeneous deformations of STO. The STO elastic constants are taken to be b_{11} = 131.33eV, b_{12} = 36.26eV and b_{44} = 41.3eV, and the lattice parameter a_{STO} = 3.901Å (ref. [42]). The elastic coupling of the STO and the PTO layers is introduced by matching the in-plane strain components of the homogeneous strain tensor in the PTO and the STO layers. At the top and the bottom interfaces of the bilayer, we impose ideal screening conditions resulting from either ambient charges or metallic electrodes[43] whereas the effects of asymmetric chemical pressure at the PTO interfaces are mimicked by an out-of-plane homogeneous electric field. For all simulations, we use 64 × 64 × 30 supercells with a 10-unit-cell STO layer and a 20-unit-cell PTO layer. Numerically, the pristine bilayer state is obtained through a temperature quench[3,30] with the in-plane lattice constants fixed to the STO bulk value and a bias field of 2×10^8 V m^{-1} during which the system is cooled from 800 K to 300 K with steps of 50 K. (It is noted that electric fields are typically overestimated in effective Hamiltonians, with such overestimation having, for example, been found to be a factor of 25 in the bismuth ferrite ($BiFeO_3$) material[44].) At each temperature, the structure is relaxed for 5,000 hybrid Monte Carlo sweeps[45]. The resulting room-temperature supercell configuration is then 'lifted' from the substrate by removing the constraint of fixed in-plane strain and performing an additional 100,000 relaxation sweeps.

Lithography process on phosphorous-doped silicon wafer

The ferroelectric bilayer was first transferred onto a phosphorous-doped silicon wafer via the same method described in Extended Data Fig. 1. After spin-coating the sample with 400 nm of polymethyl methacrylate (PMMA), the quadrate arrays (with a side of 5 μm) were defined using electron beam lithography over a 500 μm × 500 μm area. After cold development in methyl isobutyl ketone (MIBK):isopropanol (IPA) 1:3, the sample was cleaned with an IPA rinse and dried under a nitrogen stream. The PMMA was then used as a mask for ionic beam etching. After that, the PMMA was removed by acetone.

Topological characterization

To characterize the topology of the simulated polar domains, we calculated the skyrmion number N_{Sk} and the distribution of the Pontryagin

topological charge density[46] ρ_{Sk} within each (001) unit-cell plane of the PTO layer.

The charge density ρ_{Sk} is given by[47]

$$\rho_{Sk} = \frac{1}{4\pi}\mathbf{n}\bullet(\partial_x\mathbf{n}\times\partial_y\mathbf{n}), \quad (1)$$

where $\mathbf{n}$ denotes a normalized polarization vector at each point $\mathbf{R} = (x, y)$ and the skyrmion number is obtained by taking a surface integral of ρ_{Sk}, that is, $N_{Sk} = \int d\mathbf{R}\rho_{Sk}(\mathbf{R})$.

Here, we approximate the $\mathbf{n}$ vector field by a cubic lattice of the lead-centred, normalized, local mode vectors and a single ρ_{Sk} value is assigned to each unit cell using a lattice analogue of equation (1)[48]. To obtain the plane-resolved N_{Sk}, we then sum the calculated ρ_{Sk} values over all unit cells comprising a single z = constant plane.

For all planes, except the interfacial ($z = 1$) PbO layer, we find that N_{Sk} is a negative integer number, the absolute value of which corresponds to the number of centre-divergent domains. For the interfacial $z = 1$ PbO layer, we find that N_{Sk} is equal to zero.

These results suggest that a single centre-divergent polar domain carries a N_{Sk} skyrmion number of −1 in each $z \neq 1$ plane.

To confirm this idea, we now turn to the polar structure and the distribution of the Pontryagin charge density within a single centre-divergent domain. The distribution of dipoles within the first three layers above the PTO/STO interface is shown in Extended Data Fig. 6. Extended Data Fig. 6b additionally shows the distribution of the calculated ρ_{Sk} values. As can be seen, the distributions of local dipoles and ρ_{Sk} feature a quasicontinuous rotational symmetry around the central [001] axis of the domain. Moreover, for $z \geq 2$, the Pontryagin charge density distribution has a ring-like shape with its maximum located at the centre of the quasicircular 180° domain wall (Extended Data Fig. 6b). Notably, a similar distribution of ρ_{Sk} is characteristic of the polar bubble skyrmions observed in symmetric STO/PTO/STO heterostructures[4]. However, in our case, we do not observe the Bloch-like rotations of dipoles in the vicinity of the domain-wall centre[4].

Calculating the skyrmion number $N_{Sk}(R) = 2\pi\int_0^R drr\rho_{Sk}$ as a function of the distance from the central domain axis (Extended Data Fig. 6e) shows that a single centre-divergent domain can be indeed associated with an integer skyrmion number $N_{Sk} = -1$.

It is important to note that, as discussed in this paper, the interfacial dipolar structure (Fig. 3 and Extended Data Fig. 6) of the $z = 2$ layer is retained up to $z = 6$. Within this interfacial region ($1 < z < 7$), increasing z leads to an increase in the diameter of the downwards-oriented domain core and a monotonous reduction of the domain-wall width. These transformations of the dipolar structure are continuous and bear no incidence on the topology. At $z = 7$, the width of a circular domain wall reduces to about one unit cell and the diameter of the domain reaches its maximum value that no longer increases with increasing z. For $z \geq 7$, the topological characterization described above still yields $N_{Sk} = -1$ for each z = constant plane. However, in the view of approximately one-unit-cell thickness of the domain wall, such characterization loses its physical meaning. Therefore, on the basis of the presented topological characterization results, we can conclude that the centre-divergent domains are associated with an interfacial topological soliton akin to Néel magnetic skyrmions. Similar defects, called bobbers, have previously been reported in magnetic thin films[49], which have not been found in ferroelectrics before.

Interestingly, similar to magnetic bobbers, we find that the simulated centre-divergent domains feature a Bloch point located at the domain tip at $z = 1.5$.

Data availability

The data that support the plots within this paper and other findings of this study are available from the corresponding authors upon reasonable request.

Code availability

All the code or mathematical algorithm files within this paper are available from the corresponding authors upon reasonable request.

39. Rodriguez, B. J., Callahan, C., Kalinin, S. V. & Proksch, R. Dual-frequency resonance-tracking atomic force microscopy. *Nanotechnology* **18**, 475504 (2007).
40. Waghmare, U. V. & Rabe, K. M. Ab initio statistical mechanics of the ferroelectric phase transition in $PbTiO_3$. *Phys. Rev. B* **55**, 6161 (1997).
41. Zhong, W., Vanderbilt, D. & Rabe, K. M. First-principles theory of ferroelectric phase transitions for perovskites: the case of $BaTiO_3$. *Phys. Rev. B* **52**, 6301 (1995).
42. Nishimatsu, T., Grünebohm, A., Waghmare, U. V. & Kubo, M. Molecular dynamics simulations of chemically disordered ferroelectric $(Ba,Sr)TiO_3$ with a semi-empirical effective Hamiltonian. *J. Phys. Soc. Jpn* **85**, 114714 (2016).
43. Ponomareva, I., Naumov, I. I., Kornev, I., Fu, H. & Bellaiche, L. Atomistic treatment of depolarizing energy and field in ferroelectric nanostructures. *Phys. Rev. B* **72**, 140102(R) (2005).
44. Xu, B. et al. Intrinsic polarization switching mechanisms in $BiFeO_3$. *Phys. Rev. B* **95**, 104104 (2017).
45. Prokhorenko, S., Kalke, K., Nahas, Y. & Bellaiche, L. Large scale hybrid Monte Carlo simulations for structure and property prediction. *npj Comput. Mater.* **4**, 80 (2018).
46. Manton, N. & Schwarz, N. in *Topological Solitons* Ch. 3 (eds Manton, N. & Sutcliffe, P.) 506 (Cambridge Univ. Press, 2004).
47. Nahas, Y. et al. Discovery of stable skyrmionic state in ferroelectric nanocomposites. *Nat. Commun.* **6**, 8542 (2015).
48. Berg, B. & Lüscher, M. Definition and statistical distributions of a topological number in the lattice O(3) σ-model. *Nucl. Phys. B* **190**, 412–424 (1981).
49. Kiselev, N. S. Experimental observation of chiral magnetic bobbers in B20-type FeGe. *Nat. Nanotechnol.* **13**, 451–455 (2018).

Acknowledgements We thank L. Chen for discussions, and H. Huyan at UCI for assisting with the TEM experiments. This work was supported by the National Natural Science Foundation of China (grant numbers 11774153, 11861161004, 51772143, 51725203, 51721001, 11874207 and U1932115), the National Key R&D Program of China (grant numbers 2021YFA1400400 and 2020YFA0711504) and the Fundamental Research Funds for the Central Universities (0213-14380198). Y. Nie is supported by High Level Entrepreneurial and Innovative Talents Introduction, Jiangsu Province; C.A., X.Y. and X.P. acknowledge funding from the Department of Energy (DOE) under grant DE-SC0014430, and the NSF under grant number DMR-2034738. The 4D STEM experiments was conducted using facilities and instrumentation at the UC Irvine Materials Research Institute (IMRI) supported in part by the National Science Foundation through the Materials Research Science and Engineering Center programme (DMR-2011967); Researchers at the University of Arkansas acknowledge DARPA grant number HR0011727183-D18AP00010 (TEE Program), the Vannevar Bush Faculty Fellowship (VBFF) grant number N00014-20-1-2834 from the Department of Defense, and ARO grant number W911NF-21-2-0162 (ETHOS). Computations were made possible thanks to the use of the Arkansas High Performance Computing Center, HPCC resources of Nanjing University and the Arkansas Economic Development Commission. S.C. acknowledges the support of startup grants from the Department of Applied Physics at the Hong Kong Polytechnic University, the General Research Fund (grant number 15306021) from the Hong Kong Research Grant Council, the National Natural Science Foundation of China (grant number 12104381) and the open subject of the National Laboratory of Solid State Microstructures, Nanjing University (M34001).

Author contributions Y. Nie conceived the idea and directed the project with X.P., Y.C. and D.W. L.H. synthesized the samples and characterized the crystalline structure with the help of Y.F., H.L., D.J. and W.G. under the supervision of Y. Nie, X.P. and Z.G. L.H. performed the PFM and CAFM measurements and data analysis with the help of H.F. under the supervision of D.W. and Y. Nie. C.A. performed 4D STEM measurements and data analysis with the help of X.Y. under the supervision of X.P. M.W. performed the selected area electron diffraction and S/TEM measurements with the help of S.C. under the supervision of P.W. and X.P. S.P., Y. Nahas and Y.Y. performed and discussed the effective Hamiltonian model simulations under the supervision of L.B. T.W. helped with the lithography processing. Y. Nie and L.H. wrote the manuscript. All authors discussed the data and contributed to the manuscript.

Competing interests The authors declare no competing interests.

Additional information

Supplementary information The online version contains supplementary material available at https://doi.org/10.1038/s41586-021-04338-w.

Correspondence and requests for materials should be addressed to Di Wu or Yuefeng Nie.

Peer review information *Nature* thanks Matthew Dawber, Si-Young Choi and Anna Morozovska for their contribution to the peer review of this work.

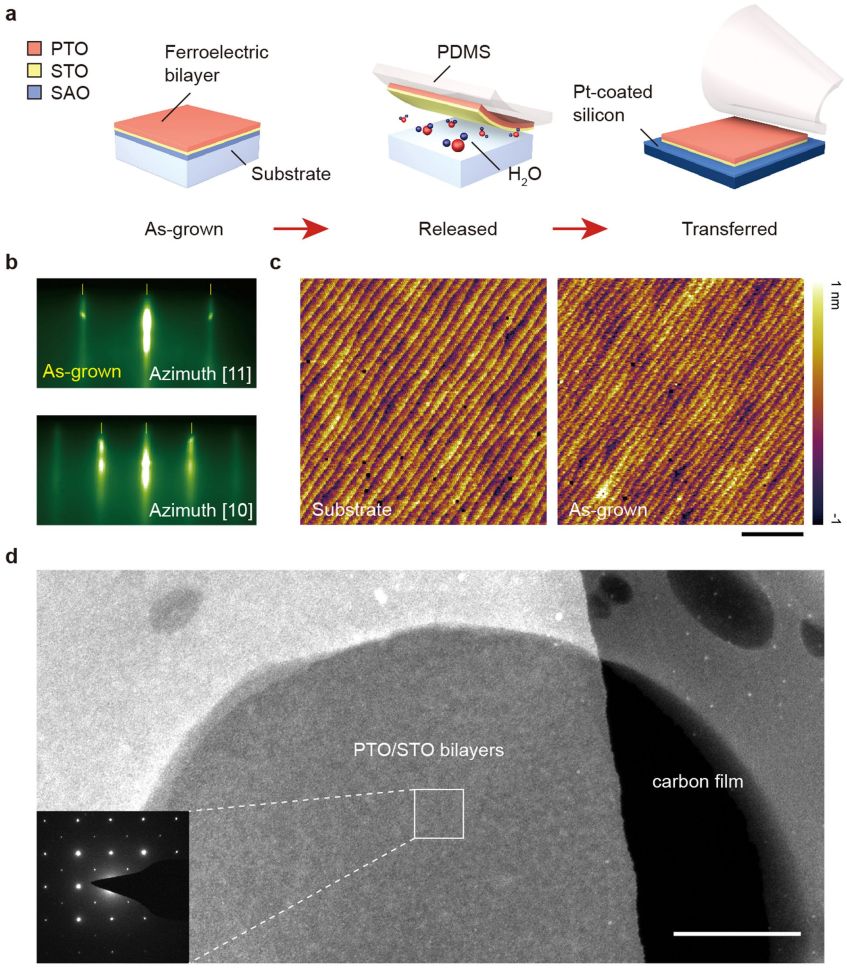

Extended Data Fig. 1 | Growth and transfer of freestanding PTO/STO bilayers. a, Schematic illustration of the process of heterostructure growth and membrane lift-off. The PTO/STO heterostructure is first grown on TiO_2-terminated (001) STO substrates with a SAO water-soluble sacrificial layer (left) and then the bilayer is attached to a supporting polymer and released from the substrate by dissolving away the SAO layer by water (middle). Finally, the bilayer is transferred onto the desired substrate (right). **b**, The Reflection High Energy Electron Diffraction (RHEED) patterns for as-grown PTO(16 u.c.)/STO(10 u.c.)/SAO(6 u.c.) film on (001) STO substrate. **c**, Atomic force microscopy characterization of (001) STO substrate (left) and as-grown films (right) showing an atomically smooth surface with unit cell step terraces. Scale bar, 1 µm. **d**, Low-magnification planar-view HADDF image of the freestanding $(PbTiO_3)_{20}/(SrTiO_3)_{10}$ bilayer transferred to a holey carbon TEM grid and selected area electron diffraction (SAED) taken along [001] zone axis (inset), showing the single-crystal structure of the bilayer. Scale bar, 1 µm.

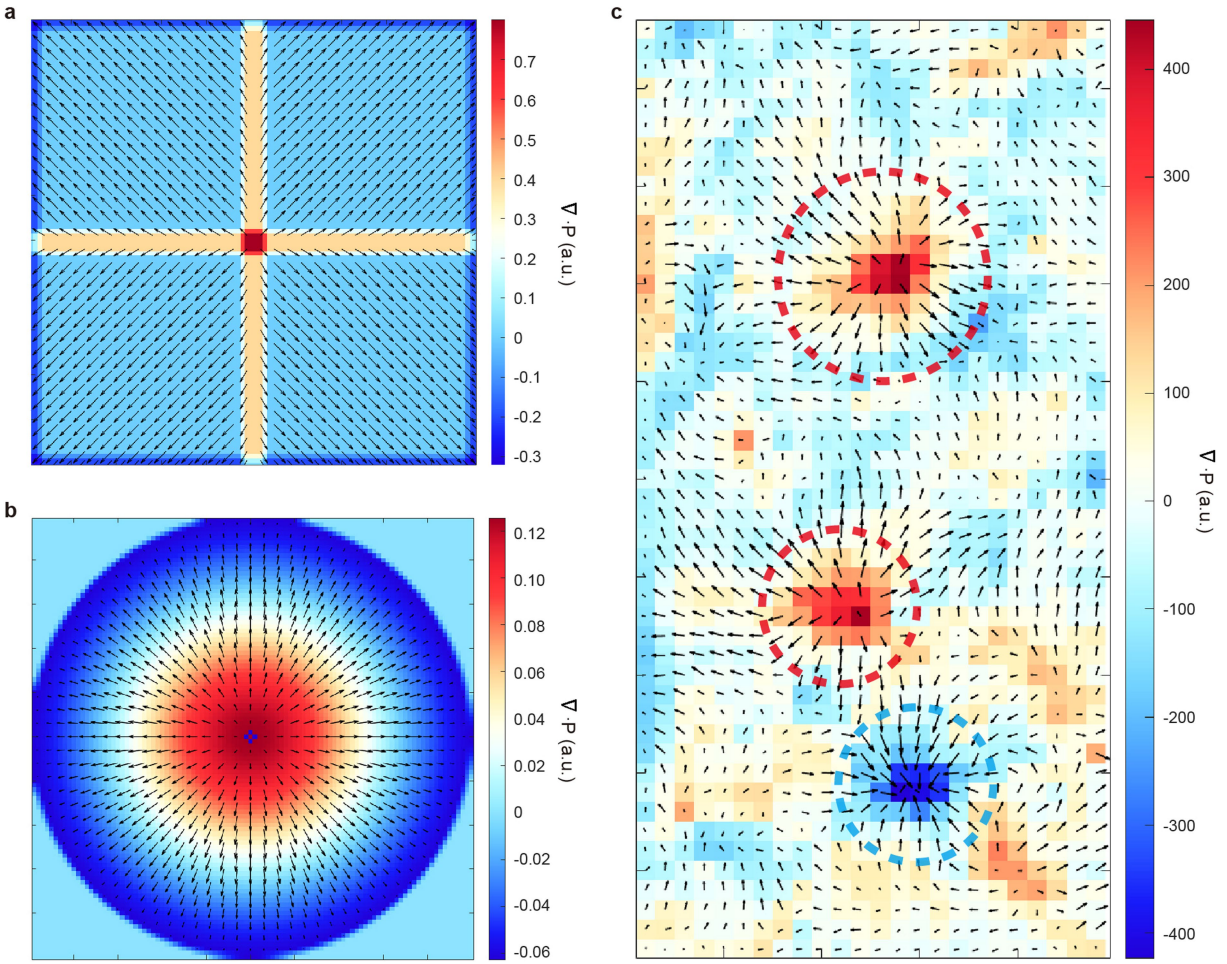

Extended Data Fig. 2 | Simulation of vector fields for two distinct divergent domains. a, Simulation of vector fields for a quad divergent domain. **b**, Simulation of vector fields for a skyrmion-like bubble domain. **c**, Calculation of the divergence from vector PFM image.

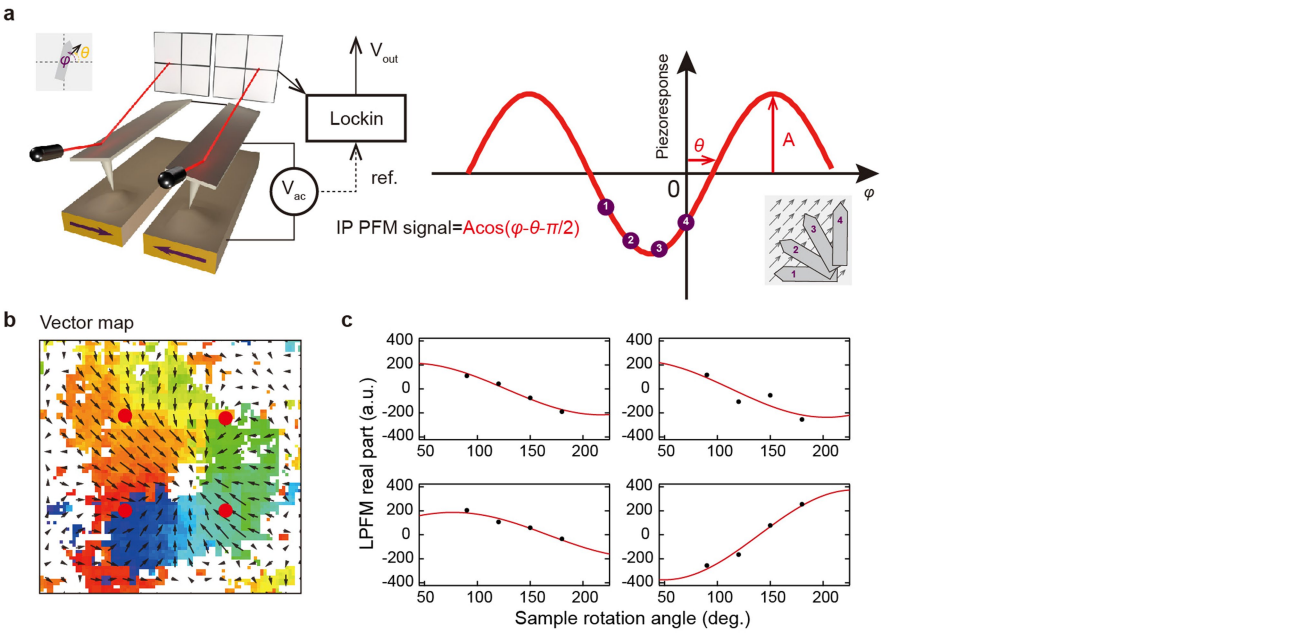

Extended Data Fig. 3 | Direct visualization of topological polar textures by vector piezoelectric force microscope (PFM). a, Schematic of angle-resolved lateral PFM. In-plane (IP) PFM real part signal was collected experimentally as a function of tip orientation angle φ and then the amplitude and the phase delay were determined by trigonometric curve fitting, i.e. A and θ in $A\cos(\varphi-\theta+\pi/2)$. Piezoresponse vector field can be constructed by finding IP vector components ($A\cos\theta$, $A\sin\theta$) as a function of position. **b**, IP piezoresponse vector map for a centre-divergent domain showing the centre-divergent nanodomain. **c**, The trigonometric curve fitting for four representative points that are denoted as red spots in **b**.

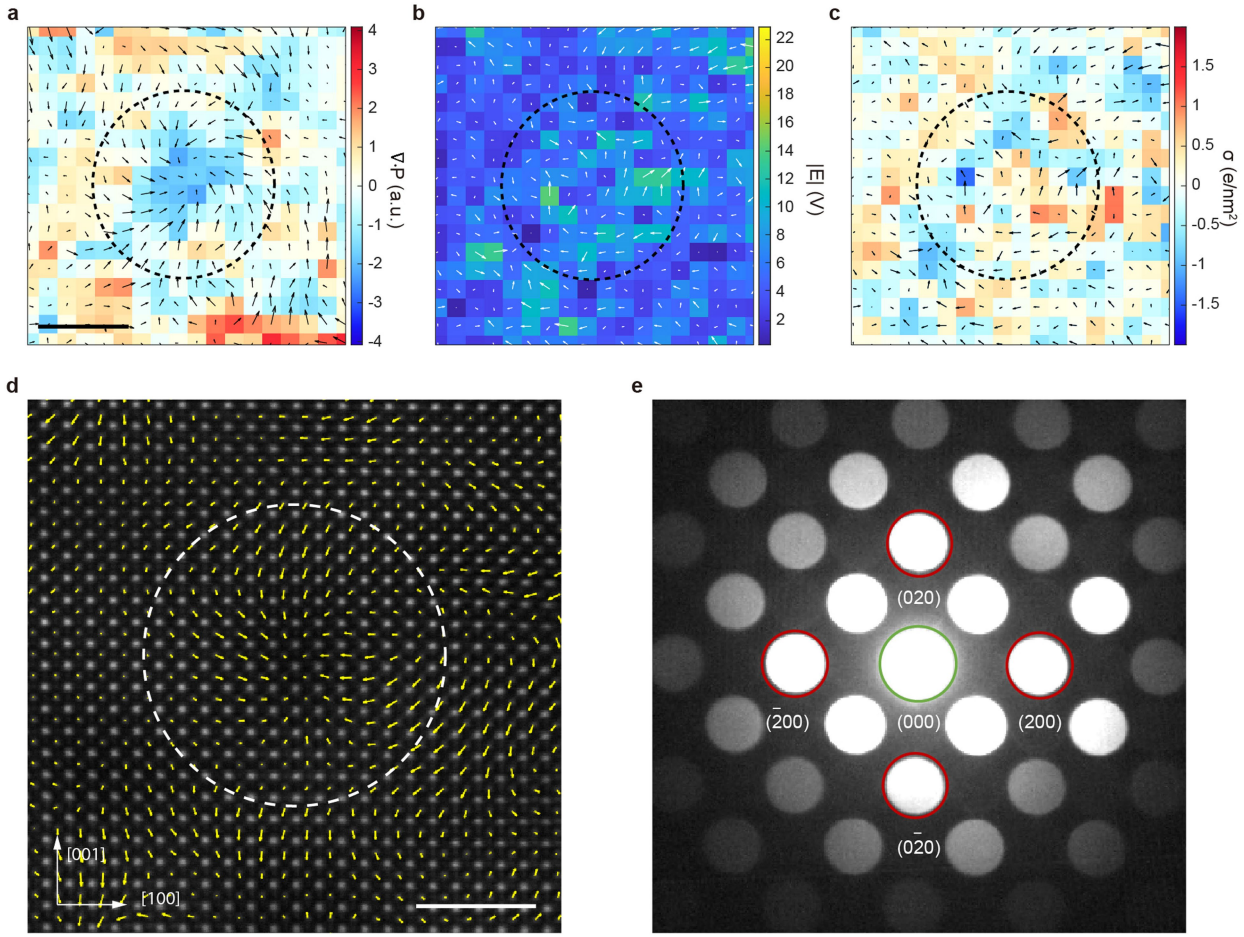

Extended Data Fig. 4 | Characterization of a centre-convergent type nanodomain. a, Polarization mapping by 4D-STEM. **b**, The projected electric field calculated from the (000) diffraction peak. **c**, The projected charge density calculated from the electric field based on Gauss's law. Scale bar, 5 nm. **d**, Atomically resolved plane-view HADDF-STEM image of the PTO_{20}/STO_{10} bilayer. Scale bar, 2 nm. **e**, The PACBED pattern extracted from the region of the centre-convergent domain shown in **a**–**c**.

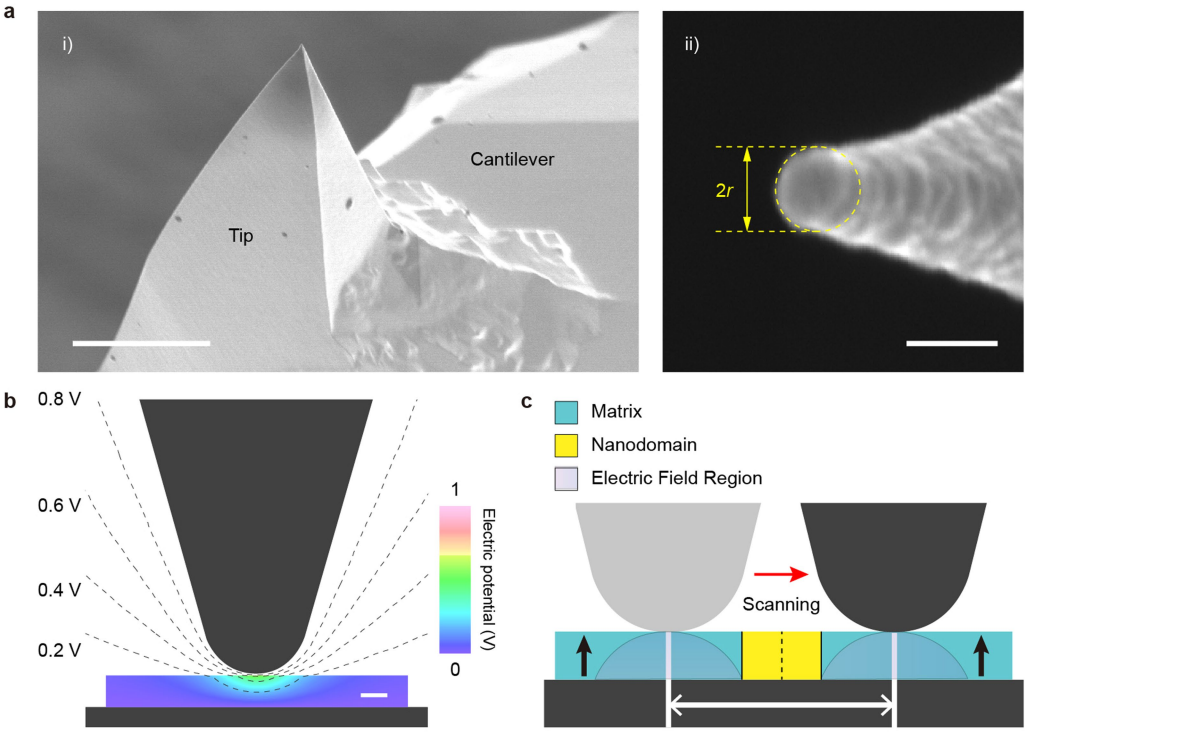

Extended Data Fig. 5 | Spatial resolution in PFM. a, i) SEM image of an unused spherelike PFM tip. Scale bar, 500 nm. ii) The radius *r* of the contact circle for a weak indentation (*h* ~ 1–2 nm) is used to characterize the radius *r* of the tip. Scale bar, 50 nm. **b**, Electric field distribution at the tip simulated by finite element modelling (FEM). Labels near the curves designate potential values. Scale bar, 10 nm. **c**, Schematic image of the PFM tip scanning across a nanodomain. The measured size is proportional to the tip radius.

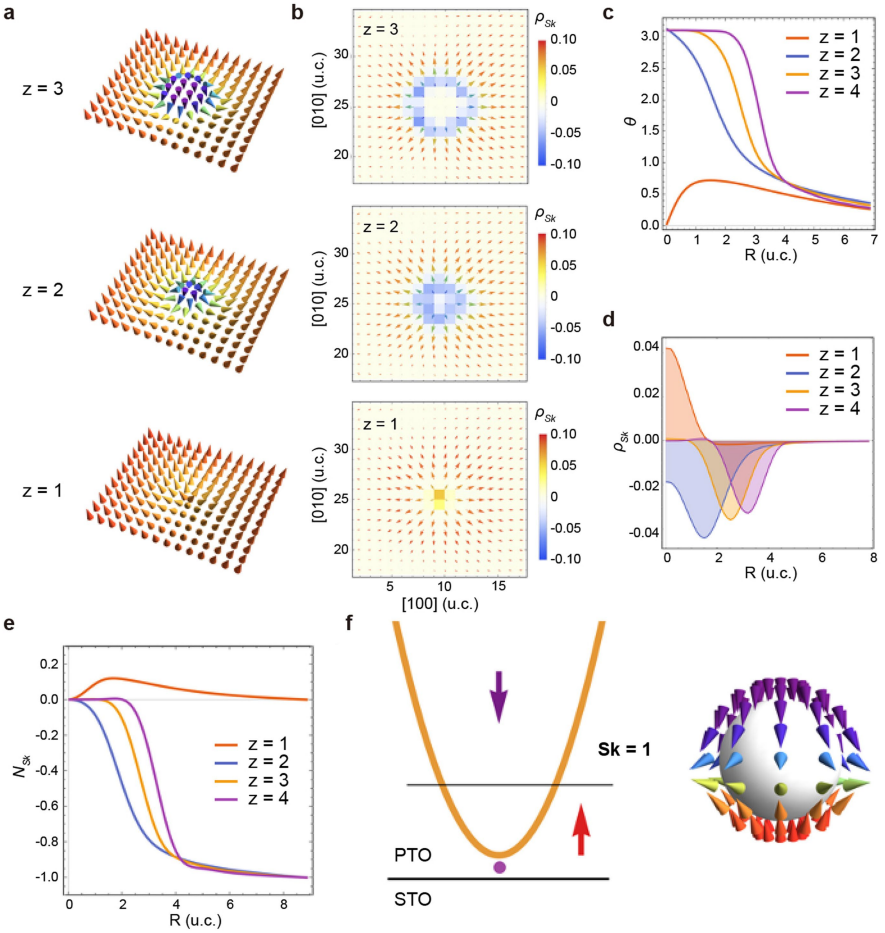

Extended Data Fig. 6 | Topological characterization of the centre-divergent domains and interfacial skyrmion-like nanodomain (polar Bobber) obtained computationally (via the effective Hamiltonian). **a**, (001)-plane resolved polar structure of the centre divergent domains in the vicinity of the STO/PTO interface. The first, second and third PTO layers counting from the interface are indicated with labels z = 1,2, and 3, respectively. **b**, The in-plane projected polar structure superimposed with the distribution of the Pontryagin topological charge density. The arrows correspond to the in-plane-projected dipoles coloured according to their out-of-plane component; red and purple colours correspond to [001] and [00−1] oriented dipoles, respectively. **c**, Dependence of the interpolated polar angle θ between the local dipole and [001] axis on the distance R from the central axis of the domain. **d**, The dependence of the interpolated Pontryagin charge density ρ_{Sk} on the distance R from the central axis of the domain. **e**, The plane-resolved Skyrmion number of a single centre-divergent domain as a function of the distance from the domain centre. **f**, Schematic illustration of the topology of centre-divergent domains (left). Each z ≥ 2 cross section of the domain reveals a 2D Néel skyrmion-like structure characterized by an integer Skyrmion number. The domain tip at the PTO/STO interface pins an anti-hedgehog-like Bloch point.

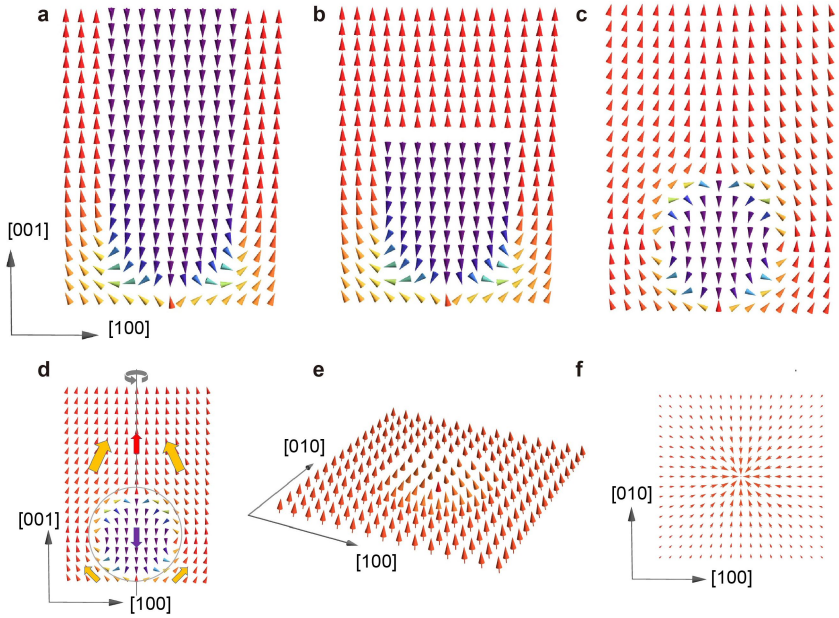

Extended Data Fig. 7 | Simulated dipolar structure of the centre-convergent domains. a, The [100]–[001] cross-section of the simulated centre-divergent domain (Néel skyrmion). **b**, Artificially prepared partially switched dipolar configuration. **c**, Cross-section of the relaxed dipolar structure of the centre-convergent domain (submerged Néel bubble). **d**, Above and below the bubble (grey circle), the local dipoles are inclined (yellow arrows) towards and away from the central revolution axis (grey line), respectively. Red (purple) arrows indicate the polarization within (above) the bubble at its axis. **e**, The in-plane distribution of the thickness-averaged polarization. **f**, In-plane projection of the thickness averaged polarization.

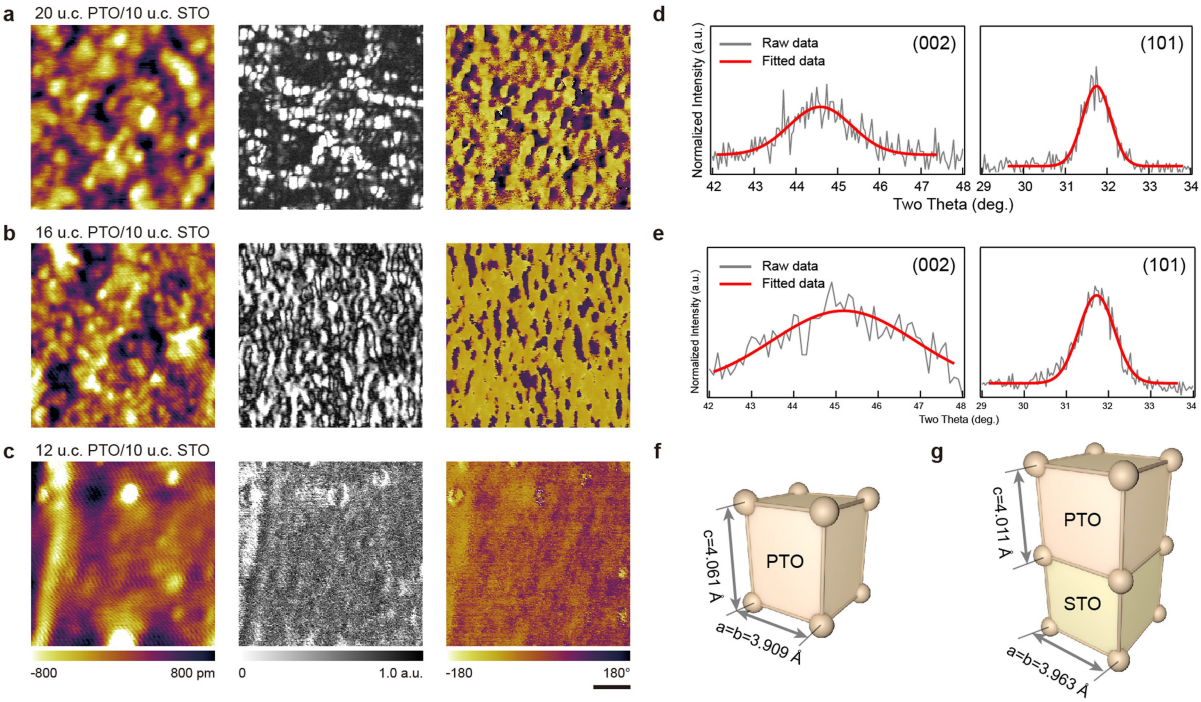

Extended Data Fig. 8 | Thickness dependence of the polar texture in PTO_n/STO_{10} (n = 12, 16, 20) bilayers transferred on silicon and crystal structures of pure freestanding PTO and PTO/STO bilayer. The surface morphology, in-plane PFM amplitude and phase images of (**a**) n = 20, (**b**) n = 16, (**c**) n = 12 bilayer films. Only the 20 u.c. PTO/10 u.c. STO shows circular shape polar textures. Scale bar, 30 nm. X-ray diffraction 2θ-ω scans around (002) (left) and (101) (right) diffraction peaks for (**d**) freestanding 20 u.c. PTO film and (**e**) freestanding $(PbTiO_3)_{20}/(SrTiO_3)_{10}$ bilayer. Schematic images showing the crystal structures of (**f**) freestanding 20 u.c. PTO film and (**g**) freestanding $(PbTiO_3)_{20}/(SrTiO_3)_{10}$ bilayer.

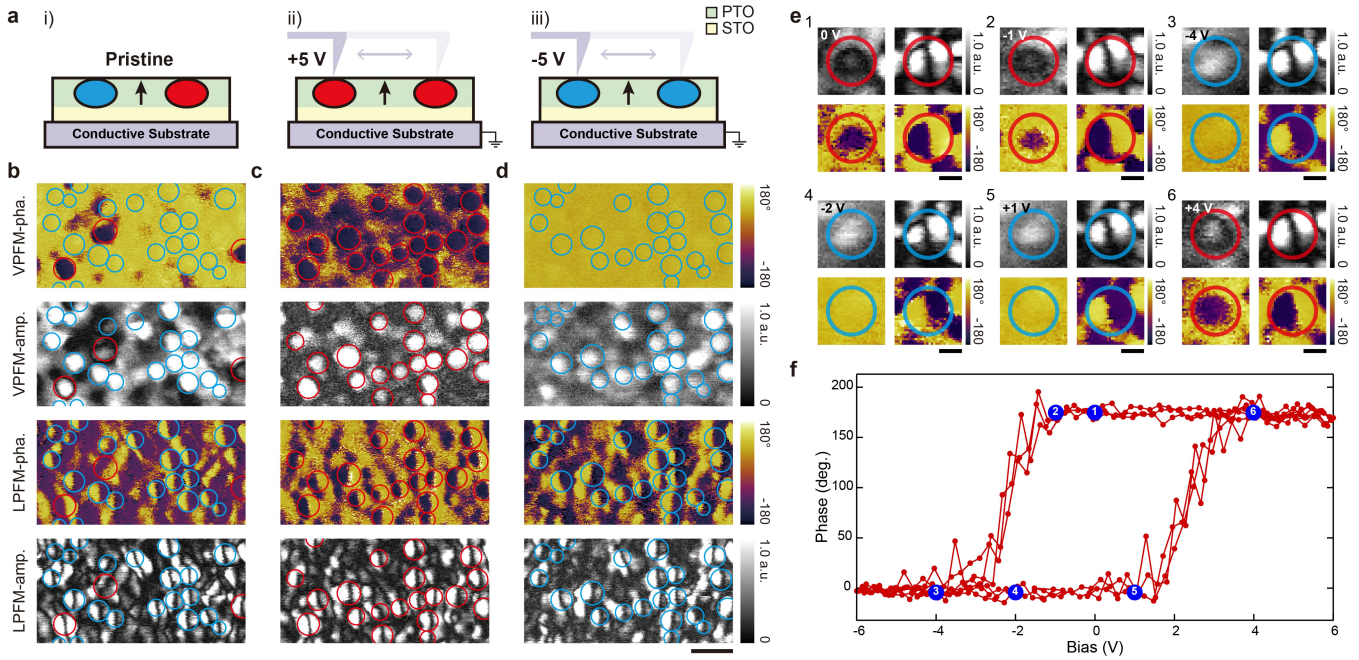

Extended Data Fig. 9 | Reversible switching of topological nanodomains. **a**, Schematic images illustrating the reversible switching of the topological domains by external electric field: The coexistence of two types of nanodomains in pristine bilayer (i) were first switched into all centre-divergent nanodomains by a scan with +5 V bias voltage (ii) and then further switched to all centre-convergent nanodomains by a scan with −5 V bias voltage (iii). **b**–**d**, Vertical PFM amplitude (VPFM-amp.), vertical phase (VPFM-pha.), lateral PFM amplitude (LPFM-amp.) and lateral phase (LPFM-pha.) images for three corresponding cases shown in (a). The centre-divergent (centre-convergent) domains are marked by red (blue) circles. Scale bar, 100 nm. **e**, VPFM-amp. (upper left), VPFM-pha. (bottom left), LPFM-amp. (upper right) and LPFM-pha. (bottom right) images taken under an a.c. amplitude of 500 mV for one single skyrmion-like polar nanodomain after applying the 0 V, −1 V, −4 V, −2 V, +1 V and +4 V DC voltage. Scale bar, 20 nm. **f**, Hysteresis loop of the skyrmion-like polar nanodomain.

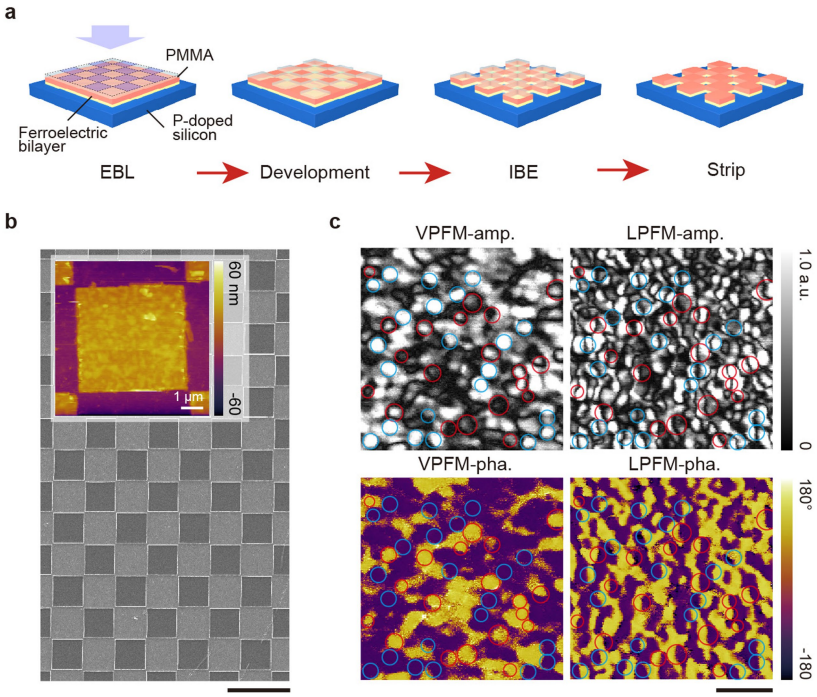

Extended Data Fig. 10 | Domain structures and switching behaviour in a PTO/STO bilayer transferred on a P-doped silicon wafer after a standard electron beam lithography process. a, Schematic images showing standard lithography process on the ferroelectric bilayer transferred on a P-doped silicon wafer. **b**, Quadrate patterns on a P-doped silicon wafer, inset shows the topography of a single piece. Scale bar, 10 μm. **c**, Vertical PFM amplitude (VPFM-amp.) and phase (VPFM-pha.), lateral PFM amplitude (LPFM-amp.) and phase (LPFM-pha.) images for the freestanding PTO_{20}/STO_{10} bilayers transferred on P-doped silicon substrate. Scale bar, 100 nm.